Nano Research

Open Access

Research Article

Nacre-like heterogeneous glass nanocomposites from interfacial assembly

Canyu Cui[1], Jian Zhu[2], Shouhua Feng[1], and Ming Yang[1]✉

[1] State Key Laboratory of Inorganic Synthesis and Preparative Chemistry, Jilin University, Changchun 130012, China
[2] School of Materials Science and Engineering, National Institute for Advanced Materials, Nankai University, Tianjin 300350, China

Cite this article: *Nano Research*, **2025**, *18*, 94907173. https://doi.org/10.26599/NR.2025.94907173

ABSTRACT: Heterogenous and gradient structures are common in biological materials and essential for achieving exceptional mechanical properties from cost-effective components. Integrating glass flakes into this design concept holds great potential for enhancing the performance of bioinspired transparent materials, particularly through a synthesis approach that allows for precise control over their structural properties. In this study, we demonstrate that glass flakes modified with silane agents can spontaneously form a surface layer at the air–liquid interface. This interfacial assembly enables the layer-by-layer embedding of highly aligned glass flakes within the polymer matrix. By varying the aspect ratios of the glass flakes during film construction, we can create a controllable gradient, nacre-like architecture that offers an enhanced balance of strength and toughness, while maintaining transparency and haze comparable to the homogeneous structures. Lamination of both homogeneous and heterogeneous composite films further enables the evaluation of bending properties. The heterogeneous structure results in a superior combination of flexural strength, bending energy, fracture toughness, and work of fracture. Finite element simulations highlight the critical role of gradient structures and repeated sequences in redistributing stress and mitigating crack propagation. The interfacial assembly of glass flakes offers a versatile platform for optimizing the performance of bioinspired transparent materials by enabling precise and flexible manipulation of microstructures.

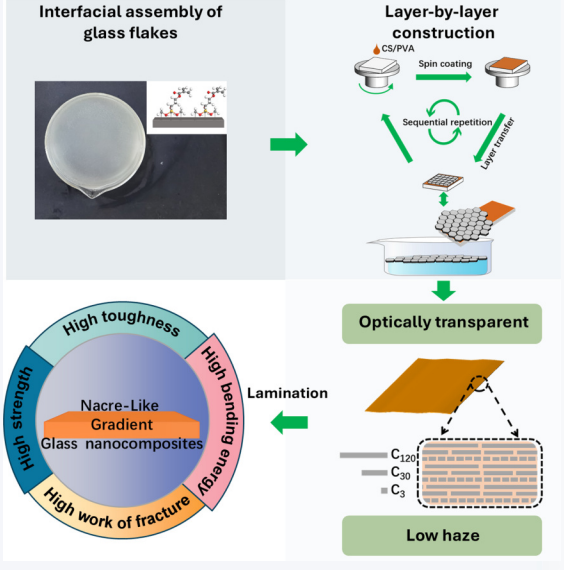

KEYWORDS: gradient structures, heterogeneous materials, nacre-like, interfacial assembly, glass nanocomposites

1 Introduction

Heterogeneous and gradient structures are common in biomineralized tissues, such as bones, teeth, and exoskeletons, where they play a crucial role in maximizing load-bearing performance [1]. The continuous variation of structural and chemical factors across different length scales optimizes stress delocalization, reducing concentration in localized areas through effective energy dissipation mechanisms [2–4]. The interface between dissimilar components is effectively strengthened and toughened by the graded structures, ensuring the high robustness of the hierarchical architecture [5]. Drawing inspiration from complex gradient biological structures that combine both stiff and soft elements, various artificial designs have been developed to replicate this unique feature. These designs not only exhibit attractive mechanical properties [6–8] but also integrate other essential characteristics, thanks to the versatility of the building blocks, making them suitable for a wide range of modern applications [9–11]. Despite advancements in the field, creating heterogeneous and gradient structures in soft functional gradient materials containing polymers often necessitates advanced processing techniques [9–13]. Understanding how these structural characteristics enhance performance relative to the homogeneous counterparts is crucial for optimizing design choices and potentially streamlining the development of more energy-efficient manufacturing processes.

Received: September 26, 2024; **Revised:** December 4, 2024
Accepted: December 5, 2024

✉Address correspondence to mingyang@jlu.edu.cn

Nacre, a well-studied biological hard tissue, has long served as a model for constructing the "brick-and-mortar" architecture [14–19]. This architecture combines strength and toughness by interfacing brittle aragonite platelets with chitin and proteins [20–23]. The same design principle has been successfully applied with various two-dimensional (2D) nanofillers, including clay [24, 25], graphene oxide [26–28], BN [29, 30], and MXene [31–33], yielding performance that often surpasses that of natural nacre [34–36]. Like bones, teeth, and exoskeletons, heterogeneous and gradient structures have been observed in nacreous shell materials, with constituent layers gradually tilting from the interior to the exterior surfaces [37]. At the nanoscale, surface asperities, the non-uniform distribution of platelets, and the size variation of nanoparticles within a platelet [38–40] further demonstrate the heterogeneity of nacre. Previous efforts to incorporate surface asperities into nacre-like nanocomposites have enhanced interfacial interactions, boosting mechanical strength, toughness, and damping properties [41, 42]. Lamination of composite films with contrasting elastic moduli, achieved using different reinforcing agents such as laponite nanoplatelets and alumina microplatelets, enabled the creation of stretchable heterogeneous composites with extreme mechanical gradients [10]. Similar lamination techniques have been applied to synthesize heterogeneous nacre-like bulk materials by varying the weight ratio of kaolin clay to alumina microplatelets from the bottom to the top [6], or by compressing cement chippings of varying sizes [43]. Interestingly, a nanoscale gradient of graphene oxide within aragonite platelets can be realized during a complex mineralization process, contributing to enhanced energy dissipation through compressive stress near the platelet surface [44]. Simulations further confirm that, compared to the homogeneous structures, gradient nacre-like materials achieve better stress distribution, leading to greater bending deformation before fracture, improved strain energy storage, and mitigation of the adverse effects of microstructural randomness [45–47].

The remarkable toughening effect of the nacre-like design can also be achieved in glass nanocomposites, derived from submicron structural features that promote crack deflection, bridging, and viscoelastic dissipation within the material's architecture [48]. This contrasts sharply with traditional glass, which, as a brittle material, cannot resist crack propagation and thus fractures catastrophically [49]. Various methods have been employed to synthesize nacre-like glass nanocomposites, including laser engraving [50], filtration [35, 49], centrifugation [51], and mechanical vibration assisted sedimentation [52]. These methods primarily aim to enhance the impact resistance of glass while maintaining relatively high transparency. Introducing heterogeneous and gradient structures into nacre-like glass nanocomposites offers a promising pathway for performance optimization. However, a more effective synthesis approach is needed to enable precise control over the local architecture. In this context, interfacial assembly presents a powerful technique, allowing for fine control over the alignment, orientation, and stacking of individual layers, and thus enabling the creation of hierarchical structures with tailored macroscopic properties [53–55]. The ability to manipulate 2D materials at the interface opens unprecedented opportunities to design complex architectures, which are often challenging to achieve using traditional fabrication methods [56–58].

In this work, we demonstrate that the interfacial assembly of glass flakes (GFs) can be used to synthesize nacre-like gradient glass nanocomposites with relatively high transmittance (62%) and ultralow haze (0.4%). Compared to the homogeneous counterparts, the gradient structures exhibit significant improvements in bending energy, fracture toughness, and work of fracture, with increases of 180%–410%, 50%–450%, and 130%–1500%, respectively. Finite element analysis (FEA) simulations highlight the critical role of gradient structures in resisting crack growth by mitigating stress localization.

2 Experimental

2.1 Materials

Glass flakes (thickness: ~ 5 μm; C_3: length = 10–20 μm, C_{30}: length = 140–160 μm, C_{120}: length = 550–650 μm; refractive index = 1.52; chemical composition: SiO_2 (65%–72%), K_2O (0%–1%), Na_2O (9%–13%), MgO (0%–5%), CaO (4%–11%), Al_2O_3 (1%–7%), Fe_2O_3 (0%–0.4%)) were kindly provided by Glassflake Ltd. Polyvinyl alcohol (PVA) (M_v = 145,000 Da), chitosan (CS, viscosity > 200 cP), (3-trimethoxysilyl) propyl methacrylate (γ-MPS, 98%) were purchased from Aladdin (China). All other chemicals used were analytical grade reagents from Aladdin (China).

2.2 Surface functionalization of glass flakes

The glass flakes were sequentially ultrasonically washed with acetone, ethanol, and deionized (DI) water to remove any impurities. After cleaning, the flakes were treated with piranha solution (a mixture of 3 parts concentrated sulfuric acid and 1 part 30 wt.% hydrogen peroxide solution) to functionalize their surface. The treated flakes were thoroughly washed with water and dried in a vacuum oven at 120 °C overnight. Following this, the dried flakes were immersed in an acetone solution of γ-MPS (10:1 volume ratio) and gently stirred with a magnetic stirrer for 12 h. Afterward, the surface-treated glass flakes were washed thoroughly with acetone and ethanol and finally dried in a vacuum oven at 110 °C for 2 h.

2.3 Preparation of chitosan-polyvinyl alcohol (CS-PVA) solution

CS was dissolved in 100 mL of a 2% acetic acid solution under vigorous stirring for at least 24 h to form a 4 wt.% CS solution. Simultaneously, 10 g of PVA was dissolved in 100 mL of DI water by heating the mixture at 90 °C for 1 h to obtain a 10 mg·mL^{-1} PVA solution. The PVA solution was then added to the CS solution under continuous stirring and mixed for 12 h to ensure a uniform blend.

2.4 Preparation of glass flakes/CS-PVA film

The CS-PVA layer was prepared by spin coating a 4 wt.% CS-PVA solution onto a glass substrate at 2000 rpm for 40 s, followed by drying at 60 °C for 30 min. Glass flakes dispersed in ethanol were slowly dropped onto the air-water interface in a 500-mL beaker until a visible surface layer formed. The glass flake film at the air-water interface was then transferred to the glass substrate coated with CS-PVA and dried at 60 °C for 30 min. Multilayered glass flake/CS-PVA composite films were fabricated by repeating this procedure. The typical films consisted of 10 bilayers of glass flakes and CS-PVA, labeled as C_3/CS-PVA, C_{30}/CS-PVA, and C_{120}/CS-PVA based on the aspect ratios of the glass flakes. $C_{120\text{-}30\text{-}3}$/CS-PVA was prepared by varying the aspect ratio of the glass flakes in each deposition cycle. The polymer volume fraction was adjusted by changing the spin-coating speed. Pure CS-PVA films were prepared using the same spin-coating method.

2.5 Film lamination

To obtain the laminated films, individual films were stacked according to the desired sequence. Each film was coated with a thin layer of CS-PVA before stacking to promote adhesion. The resulting glass flake/CS-PVA laminates were then subjected to hot pressing under 100 kPa at 60 °C for 24 h to further enhance the adhesion between each layer.

2.6 Characterization

The morphology of the samples was observed using scanning electron microscopy (SEM; Hitachi SU8020) equipped with an X-ray energy dispersive spectrometer (EDS) at an accelerating voltage of 3 kV. The samples were sputter-coated with gold to enhance conductivity. To obtain cross-sectional SEM images, different samples were fractured in liquid nitrogen. Infrared spectra were recorded using a Bruker FTIR IFS-66 V/S infrared instrument, covering a range from 400 to 4000 cm^{-1}. The samples were cut into small pieces, dried overnight in an oven at 60 °C, mixed with KBr at a mass ratio of 1:100, and pressed into transparent pellets. Thermogravimetric analysis (TGA) was conducted using a TA Instrument Netzsch STA 449 F5 (Germany) under an oxygen atmosphere, with a heating rate of 10 °C·min^{-1}. The transmittance and haze of the films were measured using an ultraviolet spectrometer (PE Lambda 950), with the films positioned vertically to the incident light. Diffuse transmittance ($T_{diffuse}$), which measures light deviating by more than 2.5° from the incident light, and total diffuse transmission ($T_{total\ diffuse}$) were recorded and used to calculate haze [35],

$$\text{Haze}\ (\%) = \frac{T_{\text{diffuse}}}{T_{\text{total diffuse}}} \times 100\% \quad (1)$$

2.7 Mechanical testing

Tensile and flexural tests were performed using a universal testing machine (WDW-1T) equipped with a 100 N load cell, operating at a deformation rate of 2 mm/min. For the tensile tests, the film samples were cut to a length of 8 mm. For the flexural tests, the samples measured approximately 25 mm in length, 2 mm in width, and 1.6 mm in thickness. The specimens were tested with a 15 mm support span, and at least five samples of each material type were tested to ensure reproducibility.

Fracture toughness was determined using the three-point bending test on single-edge notched beam (SENB) samples with a span (S) of 15 mm, conducted at a crosshead speed of 0.06 mm/min. The SENB specimens measured 25 mm in length, 2 mm in width, and 2 mm in thickness, with a single-edge notch approximately 50% of the beam's width, created using a 150 μm-thick diamond blade. A small tip was then added to the notch using a thin blade for precise crack initiation.

The bending strength (σ), strain (ε), and crack-initiation toughness (K_{IC}) were calculated from the following formulae

$$\sigma = \frac{3PS}{2WB^2} \quad (2)$$

$$\varepsilon = \frac{6DB}{S^2} \quad (3)$$

$$K_{IC} = \frac{PS}{BW^{3/2}} f\left(\frac{a}{W}\right) \quad (4)$$

$$f\left(\frac{a}{W}\right) = \frac{3\left(\frac{a}{W}\right)^{\frac{1}{2}}\left[1.99 - \left(\frac{a}{W}\right)\left(1-\frac{a}{W}\right)\left(2.15 - 3.93\left(\frac{a}{W}\right) + 2.7\left(\frac{a}{W}\right)^2\right)\right]}{2\left(1+2\frac{a}{W}\right)\left(1-\frac{a}{W}\right)^{\frac{3}{2}}} \quad (5)$$

where P is the maximum applied load, S is the support span, B and W are the thickness and width of the specimen, respectively, D is the bending deflection, and a is the notch depth [35, 49]. Each final value was calculated as the average of five measurements.

The work of fracture (WOF) was calculated as follows:

$$\text{WOF} = \frac{U}{2B(W-a)} \quad (6)$$

where U is the area under the load-displacement curve in the SENB test, and W, a, and B are the width, initial crack length, and depth of the SENB sample, respectively [51].

2.8 FEA simulation

The FEA simulation was performed to estimate stress and strain distribution. The representative volume element (RVE) of the overall structure was created using SolidWorks software. The cuboids, representing glass flakes with different aspect ratios, were embedded within the polymer matrix. For simulating different glass flakes (C_{120}, C_{30}, and C_3), the cuboid dimensions were set as 9.1 mm × 0.27 mm × 0.27 mm, 4.5 mm × 0.27 mm × 0.27 mm, and 0.81 mm × 0.27 mm × 0.27 mm (length × width × thickness), respectively. The thickness of the polymer layers remained consistent in both the horizontal (0.09 mm) and vertical directions (0.054 mm).

Material properties were as follows: the density of glass flakes and CS-PVA were set to 2500 and 1400 kg·m^{-3}, respectively. The Young's modulus of the polymer matrix was 0.6 GPa, and its Poisson's ratio was 0.4. The Young's modulus of the glass flakes was 70 GPa, and Poisson's ratio was 0.22. All contact areas within the model were assumed to be perfectly bonded.

For simulating tensile stretching, an external force of 24 N was applied to one end, while the other end was fixed. In the bending simulation, the distance between the two fixed supports was set at 4.5 mm. Both the notched and unnotched three-point bending processes were simulated using the nonlinear dynamic finite element module (Explicit Dynamics). The indenter head and support were modeled as rigid bodies, with friction contact between the indenter head and the sample surface. The friction coefficient was set to 0.1.

All models were imported into the Ansys Workbench for calculation. The tetrahedral element mesh with a size of 0.09 mm was adopted, and the mesh around the notch was refined to 0.045 mm, with an influence sphere of 0.54 mm. During the bending test, the maximum displacement of the indenter head was set to 0.09 mm (for unnotched) and 0.045 mm (for notched). Simulations were conducted under standard Earth gravity conditions. The displacement-load curve was then extracted from the simulation results.

3 Results and discussion

3.1 Interfacial assembly

C-glass flakes with three different aspect ratios, denoted as C_3, C_{30},

and C_{120}, were used in this study, where the numbers correspond to the aspect ratios of the glass flakes (Fig. 1(a) and Fig. S1 in the Electronic Supplementary Material (ESM)). These types of glass flakes, which are much cheaper than extra corrosion resistant (ECR) glass flakes used in previous reports [35, 49, 51, 52], were modified by sonication in an ethanolic solution containing carbonyl-terminated silane (γ-MPS). Silane coupling on the glass surface was confirmed by IR spectroscopy, which showed additional peaks at 2960, 1720, and 1410 cm^{-1} after silanization. These peaks are attributed to the stretching vibration of $–CH_2$ [59], C=O [60] and the bending vibration of $–CH_3$ [61] from γ-MPS, respectively (Fig. 1(b)). The successful silanization also resulted in an intensity reduction of peaks around 3270–3600 and 1450 cm^{-1}, corresponding to the stretching and bending vibrations of –OH from the glass flakes (Fig. 1(b)) [62]. The peaks at 1173 and 1170–1060 cm^{-1} correspond to the vibrations of Si–O–C (Fig. 1(b)) [63].

When the ethanolic solution of γ-MPS-modified glass flakes was slowly dropped onto water, a surface layer spontaneously formed at the air–water interface (Fig. 1(c)). The hydrophobic end of γ-MPS minimizes the interfacial energy by exposing to the air, promoting assembly at the interface (Fig. 1(c), inset). This assembled surface layer was easily transferred onto a polymer-coated glass substrate, resulting in a highly uniform packing of glass flakes (Fig. 1(d)). The polymer matrix used was CS-PVA, with a typical molar ratio of 1:1. Repeated sequential deposition of CS-PVA and glass flakes (Fig. 1(e)) led to the formation of nanocomposites with a nacre-like architecture, typically consisting of 10 bilayers of glass flakes and CS-PVA. Cross-sectional SEM images revealed highly aligned glass flakes embedded in the CS-PVA matrix, with a thickness of approximately 110 μm (Fig. 1(f) and Fig. S2 in the ESM). TGA analysis showed that the polymer matrix content in the nacre-like glass nanocomposites was approximately 63%, regardless of the glass flakes' aspect ratios (Fig. S3 in the ESM). EDS mapping confirmed the homogeneous distribution of Si, Ca, C, O, and N elements, consistent with the composition of the glass flakes (Fig. S4 in the ESM).

3.2 Tensile and optical properties

Tensile tests revealed that the aspect ratios of glass flakes significantly influence the mechanical properties of nacre-like glass nanocomposites. For C_{120}/CS-PVA, the ultimate strength, strain, and modulus were 102.1 ± 15.3 MPa, 2.3 ± 0.2 GPa, and 6.2% ± 0.8%, respectively (Figs. 2(a) and 2(b)). In the case of C_{30}/CS-PVA, the ultimate strength and strain increased to 125.4 ± 14.8 MPa and 13.3% ± 2.2%, respectively, while the modulus decreased to 1.5 ± 0.3 GPa (Figs. 2(a) and 2(b)). C_3/CS-PVA exhibited the lowest ultimate strength (60.2 ± 6.4 MPa) and modulus (0.9 ± 0.3 GPa), but the largest strain (49.8% ± 7.4%) (Figs. 2(a) and 2(b)). All glass nanocomposites demonstrated enhanced strength and modulus compared to the pure CS-PVA matrix (Fig. S5 in the ESM).

The strong interfacial interactions between the silane-grafted glass flakes and the hydroxyl/amine groups in CS-PVA facilitated effective load transfer from the organic matrix to the glass flakes. This was confirmed by IR spectroscopy, where the peaks in the range of 3000–3600 cm^{-1}, attributed to the vibrations of –NH and –OH groups in CS-PVA [64] (Fig. 2(c)), showed a slight redshift from 3275 to 3268 cm^{-1} in C_{30}/CS-PVA. Additionally, compared to γ-MPS-modified glass flakes (Fig. 2(c)), the IR peak associated with the C=O vibrations [60] in C_{30} redshifted from 1720 to 1715 cm^{-1} in C_{30}/CS-PVA, indicating the formation of hydrogen bonds between the silanes and CS-PVA.

The shear-lag model calculates the strength of composites reinforced by platelets by

$$\sigma_c = \alpha V_p \sigma_p + (1 - V_p)\sigma_m \quad (7)$$

where V_p is the volume fraction of the platelets, σ_c is the tensile strength of the composite, σ_p and σ_m are the tensile strengths of the platelets and the matrix, respectively. The pre-factor α depends on the mechanism of failure (Fig. 2(d)):

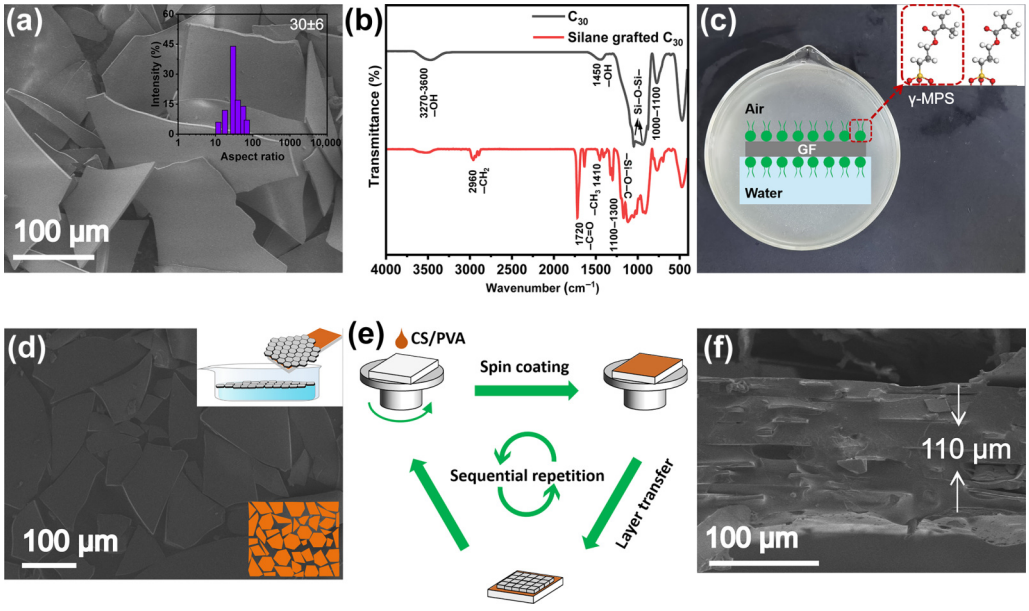

Figure 1 Interfacial assembly and the synthesis of nacre-like glass nanocomposites. (a) An SEM image of glass flakes (C_{30}) and the corresponding statistical analysis of aspect ratio (inset). (b) FTIR spectra of C_{30} and silane grafted C_{30}. (c) An optical image of glass flakes self-assembled at the air–water interface. The inset shows the grafting of γ-MPS on the surface of glass flakes. (d) An SEM image of C_{30} after being transferred to the surface of a polymer-coated substrate. The inset in the upper right corner shows the transfer process and in the lower right corner is the schematic illustration of the packing of glass flakes. (e) Schematic illustration of the repeated sequential deposition of CS-PVA and glass flakes. (f) A cross-sectional SEM image of C_{30}/CS-PVA.

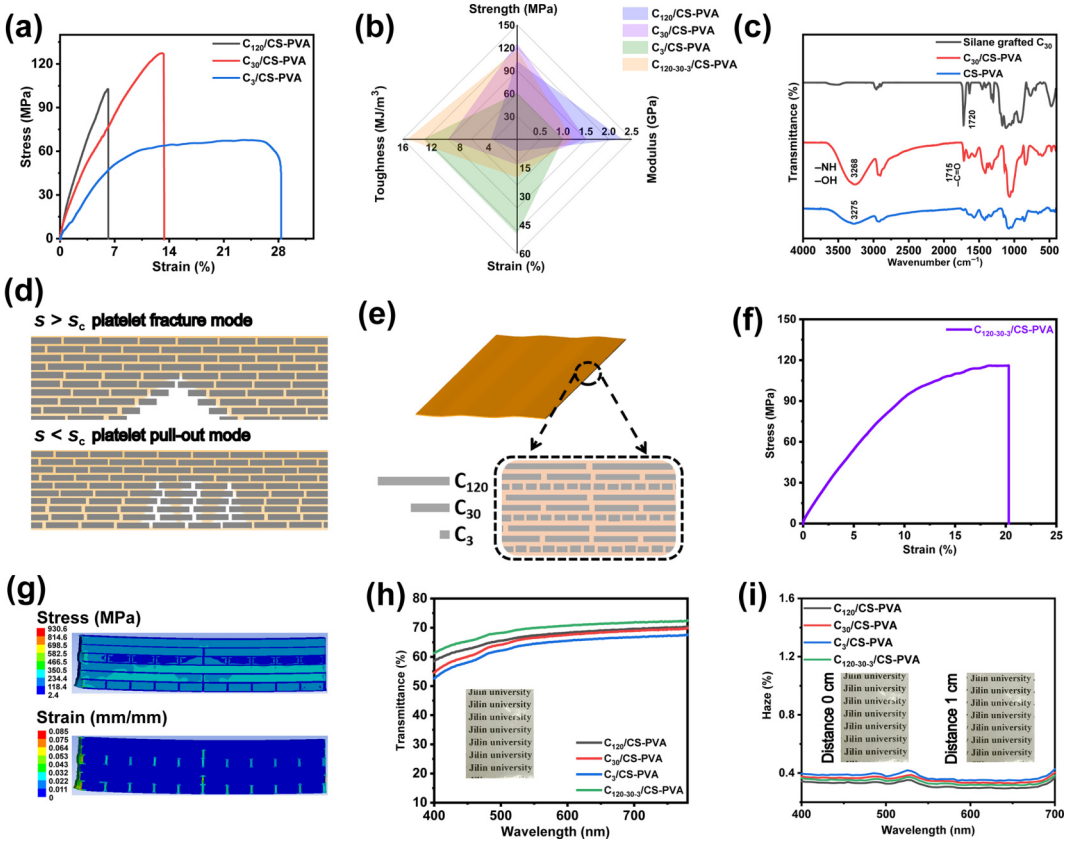

Figure 2 Tensile and optical properties of glass nanocomposite films. (a) Representative stress–strain curves of C_{120}/CS-PVA, C_{30}/CS-PVA, and C_3/CS-PVA. (b) Tensile strength, strain, modulus and toughness of C_{120}/CS-PVA, C_{30}/CS-PVA, C_3/CS-PVA, and $C_{120\text{-}30\text{-}3}$/CS-PVA. (c) FTIR spectra of silane grafted C_{30}, C_{30}/CS-PVA, and CS-PVA. (d) Schematic illustration of different fracture modes according to the shear-lag model. (e) Schematic illustration of the structure of $C_{120\text{-}30\text{-}3}$/CS-PVA. (f) The representative stress–strain curve of $C_{120\text{-}30\text{-}3}$/CS-PVA. (g) Stress (top) and strain (bottom) distributions of $C_{120\text{-}30\text{-}3}$/CS-PVA during uniaxial stretching visualized by the FEA simulation. (h) Transmittance and (i) haze of C_{120}/CS-PVA, C_{30}/CS-PVA, C_3/CS-PVA, and $C_{120\text{-}30\text{-}3}$/CS-PVA. The inset in h shows the high readability of the paper covered by $C_{120\text{-}30\text{-}3}$/CS-PVA, while the inset in i illustrates the low haze by comparing the readability of the paper underneath $C_{120\text{-}30\text{-}3}$/CS-PVA with a 0 or 1 cm distance. The thickness of these composite films is ca. 110 μm.

$$\alpha = 1 - \frac{\sigma_p}{2\tau_y s} \quad \text{for } (s > s_c) \qquad \text{for platelet rupture} \tag{8}$$

$$\alpha = \frac{\tau_y s}{2\sigma_p} \quad \text{for } (s < s_c) \qquad \text{for platelet pull-out} \tag{9}$$

where τ_y is the yield shear strength of the polymer, s is the aspect ratio of the platelet, and $s_c = \sigma_p/\tau_y$ is the critical aspect ratio, at which the failure mode transitions from the brittle rupture of the platelet to its pull-out from the matrix.

Glass flakes have an estimated tensile strength (σ_p) of approximately 3.4 GPa [65], while the polymer matrix of CS-PVA has a yield shear strength (τ_y) of around 50 MPa [55], yielding a s_c of approximately 68. Therefore, according to the shear-lag model, for C_3 and C_{30} composites, the failure mode involves platelet pull-out. This is supported by the observations of the fractured cross-sections of C_3/CS-PVA (Fig. S6(a) in the ESM) and C_{30}/CS-PVA (Fig. S6(b) in the ESM). A few pores and voids between the flakes and the matrix were observed post-rupture. Such phenomena are consistent with the debonding between the glass flakes and the CS-PVA matrix during the platelet pull-out (Fig. S6(c) in the ESM). However, for C_{120}/CS-PVA, the aspect ratio exceeds s_c, leading to a failure mode based on platelet rupture. Indeed, a clean surface was captured due to the failure of glass flakes in a brittle fracture (Fig. S6(d) in the ESM). Consequently, due to the absence of an energy dissipation mechanism in C_{120}/CS-PVA, it exhibited the lowest toughness of 3.6 ± 1.0 MJ·m^{-3}. In contrast, the toughness increased to 9.6 ± 3.8 MJ·m^{-3} for C_{30}/CS-PVA and 13.1 ± 4.1 MJ·m^{-3} for C_3/CS-PVA (Fig. 2(b)). The contribution of the polymer matrix to toughness was further confirmed by varying the polymer content, which was controlled by adjusting the rotation rate during deposition. For instance, increasing the polymer content to 75% (Fig. S7 in the ESM), resulted in a toughness of 17.4 ± 4.9 MJ·m^{-3}, but this also led to a noticeable reduction in strength (65.1 ± 11.5 MPa) (Fig. S8 in the ESM).

The mechanical properties of glass nanocomposites can be further tuned by creating heterogeneous structures that leverage the interfacial assembly of glass flakes. Instead of using a single type of glass flakes, different aspect ratios—C_{120}, C_{30}, and C_3—can be introduced sequentially (Fig. 2(e)). The resulting $C_{120\text{-}30\text{-}3}$/CS-PVA exhibited an ultimate strength of 116.7 ± 16.4 MPa (Fig. 2(f)), which is only slightly lower than that of C_{30}/CS-PVA (125.4 ± 14.8 MPa). However, its toughness is significantly higher, reaching 15.3 ± 4.9 MJ·m^{-3}, which is 1.6 times greater than that of C_{30}/CS-PVA (9.6 ± 3.8 MJ·m^{-3}) (Fig. 2(b)). Notably, this toughness is even greater than that of C_3/CS-PVA (13.1 ± 4.1 MJ·m^{-3}) (Fig. 2(b)), while maintaining much higher ultimate strength (Fig. 2(f)).

The toughness of $C_{120\text{-}30\text{-}3}$/CS-PVA is 8 times higher than that of nacre (1.8 MJ·m^{-3}) [19], while the strength is comparable (Fig. S9 in the ESM). The combination of strength and toughness in this

composite is on par with previously reported nacre-like nanocomposites made with graphene oxide (GO) [66], boron nitride nanosheets (BNNS) [67], montmorillonite (MTM) [68], and layered double hydroxides (LDHs) [69, 70] but outperforms GFs compounded with PVA [71] (Fig. S9 in the ESM). FEA simulations (Fig. S10 in the ESM) indicated that during uniaxial stretching of $C_{120\text{-}30\text{-}3}$/CS-PVA, the stress is not only concentrated in the C_{120} flakes but is also distributed across the flakes with smaller aspect ratios, preventing stress concentration (Fig. 2(g)). Furthermore, the polymer matrix between the smaller glass flakes in the vertical direction bears most of the strain (Fig. 2(g)), enabling significant deformation.

The optical transmittance of nacre-like nanocomposites varies across different compositions, with values of approximately 54%, 56%, 60%, and 62% at 400 nm for C_3/CS-PVA, C_{30}/CS-PVA, C_{120}/CS-PVA, and $C_{120\text{-}30\text{-}3}$/CS-PVA, respectively (Fig. 2(h)). The transmittance gradually increases with larger wavelengths in the visible range. At 700 nm, the transmittance is about 67%, 69%, 70%, and 72% for C_3/CS-PVA, C_{30}/CS-PVA, C_{120}/CS-PVA, and $C_{120\text{-}30\text{-}3}$/CS-PVA, respectively. The haze for all glass nanocomposites remains below 0.4% (Fig. 2(i)). These transmittance values are comparable to those of other nacre-like glass nanocomposites [35, 49–52], but the haze is significantly lower (Table S1 in the ESM), indicating minimal light scattering and a smooth surface within the films. The ultralow haze can be attributed to the interfacial assembly, which enhances the 2D packing of glass flakes, thereby reducing density variations and minimizing defects such as porosity. Additionally, the larger size of the glass flakes, compared to previous work [35, 49, 51, 52], generates fewer scattering sites at the interface, further contributing to the ultra-low haze.

3.3 Laminated glass nanocomposites

To investigate the bending properties of nacre-like glass nanocomposites, thin films were stacked to form thick laminates (Fig. 3(a)). Compressive stress of 100 kPa was applied at 60 °C to enhance bonding between layers, resulting in a uniform laminate thickness of approximately 1.6 mm without interfacial delamination. Both homogeneous (Fig. 3(b) and Fig. S11 in the ESM) and heterogeneous (Fig. 3(c)) laminates were successfully fabricated using this method. The mechanical properties of the laminates were assessed using three-point bending tests. For C_{30}/CS-PVA, a linear elastic deformation was observed until the strain reached approximately 4%, followed by plastic deformation (Fig. 3(d)), with a flexural strength of 93.4 ± 9.9 MPa, a modulus of 2.6 ± 0.5 GPa, and a bending energy of 3.1 ± 0.9 MJ·m^{-3}, which is defined as the area under the deflection curve until the maximum strength is achieved [72]. C_3/CS-PVA exhibited similar deformation behavior, with a flexural strength of 63.3 ± 13.6 MPa, a modulus of 2.7 ± 1.3 GPa, and a bending energy of 2.0 ± 0.8 MJ·m^{-3}. In contrast, for C_{120}/CS-PVA, failure occurred abruptly at the maximum strength, with a maximum bending strain of only about 4.7%. Despite this, it exhibited the highest flexural strength of 121.1 ± 16.7 MPa and bending energy of 3.6 ± 0.8 MJ·m^{-3}, among the three homogeneous nanocomposites, with a modulus of 4.0 ± 0.4 GPa.

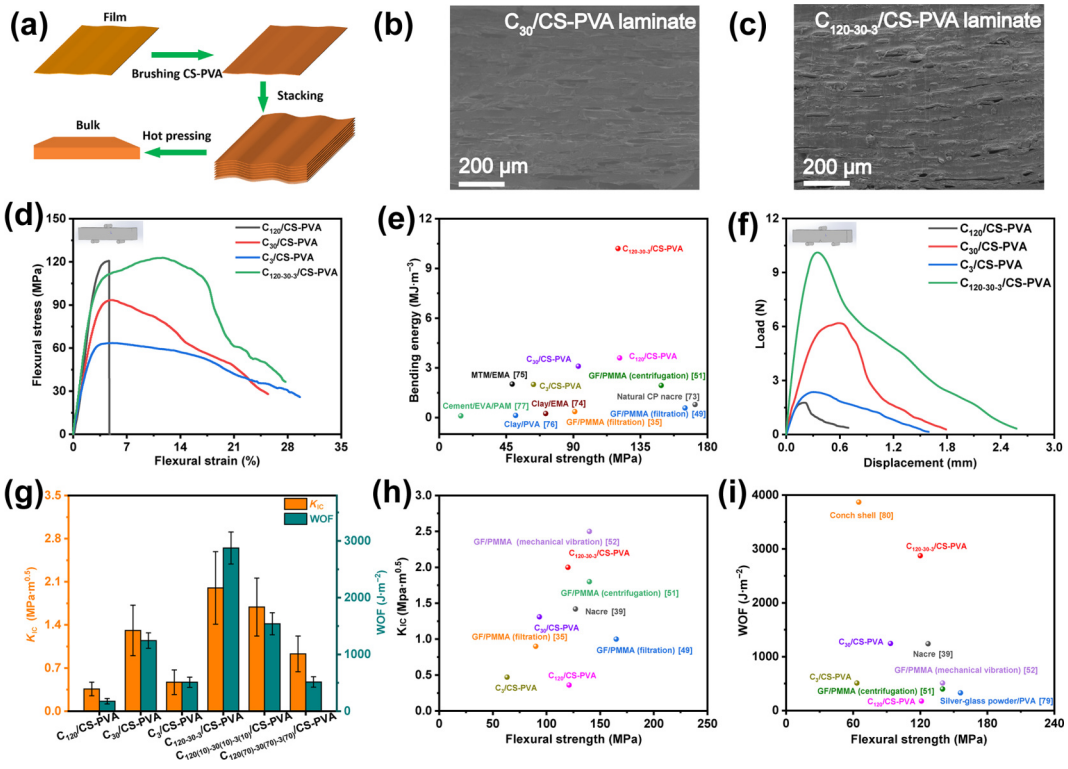

Figure 3 Laminates of glass nanocomposites and their bending properties. (a) Schematic illustration of the fabrication process of laminates. Cross-sectional SEM images of laminated (b) C_{30}/CS-PVA and (c) $C_{120\text{-}30\text{-}3}$/CS-PVA. (d) Flexural stress–strain curves of C_{120}/CS-PVA, C_{30}/CS-PVA, C_3/CS-PVA, and $C_{120\text{-}30\text{-}3}$/CS-PVA. (e) The Ashby plot of flexural strength and bending energy of both homogenous and heterogeneous glass nanocomposites [35, 49, 51] as well as other nacre-like nanocomposites [74–77] and nacre [73]. (f) Load–displacement curves from the SENB test and (g) K_{IC} and WOF for C_{120}/CS-PVA, C_{30}/CS-PVA, C_3/CS-PVA, $C_{120\text{-}30\text{-}3}$/CS-PVA, $C_{120(10)\text{-}30(10)\text{-}3(10)}$/CS-PVA, and $C_{120(70)\text{-}30(70)\text{-}3(70)}$/CS-PVA. The Ashby plot of (h) flexural strength and K_{IC} and (i) flexural strength and WOF of both homogenous and heterogeneous glass nanocomposites from this work as well as other nacre-like glass nanocomposites obtained using different methods [35, 49, 51, 52, 79], nacre [39] and conch shell [80].

In contrast to the three homogeneous laminates, the flexural stress-strain curve of $C_{120\text{-}30\text{-}3}$/CS-PVA showed a noticeable upturn in stress after the initial linear deformation region, followed by force-declining plastic deformation (Fig. 3(d)). As a result, $C_{120\text{-}30\text{-}3}$/CS-PVA exhibited a flexural strength of 120.1 ± 17.6 MPa, a modulus of 3.5 ± 0.6 GPa, and a bending energy of 10.2 ± 2.0 MJ·m^{-3}, significantly outperforming the homogeneous structures (Fig. 3(e)). When compared to nacre [73] and other nacre-like nanocomposites, such as clay/ethylene-methyl acrylate copolymer (EMA) [74, 75], clay/PVA [76], cement/ethylene vinyl acetate (EVA)/polyacrylamide (PAM) [77], and GF/polymethyl methacrylate (PMMA) (Fig. 3(e)) [35, 49, 51], $C_{120\text{-}30\text{-}3}$/CS-PVA demonstrated a similar flexural strength but achieved an order of magnitude higher bending energy.

SEM observations of the fractured section of C_{120}/CS-PVA after three-point bending tests revealed that the predominant failure mechanism is the breakage of glass flakes, which primarily resists bending (Fig. S12(a) in the ESM), consistent with the nearly linear deformation curve (Fig. 3(d)). In C_{30}/CS-PVA, the cracks deviated and branched when encountering the interface (Fig. S12(b) in the ESM). In this way, the material gets additional ductility for toughening. For C_3/CS-PVA, much smaller cracks were observed, which were more evenly distributed across the cross-section (Fig. S12(c) in the ESM). Such microcracking can be effective for preventing catastrophic failure by acting as stress relievers before the formation of the main crack. These mechanisms contribute synergistically to the heterogeneous laminates, ensuring a balance of high flexural strength and bending energy.

The use of notched specimens in the bending test provided insights into the material's resistance to crack initiation (K_{IC}) (Fig. 3(f)). The K_{IC} of $C_{120\text{-}30\text{-}3}$/CS-PVA was measured at 2.0 ± 0.6 MPa·m$^{1/2}$, which is comparable to nacre (~ 2.1 MPa·m$^{1/2}$) [39], and significantly higher than the homogeneous nanocomposites (C_{120}/CS-PVA: 0.4 ± 0.1 MPa·m$^{1/2}$, C_{30}/CS-PVA: 1.3 ± 0.4 MPa·m$^{1/2}$, and C_3/CS-PVA: 0.5 ± 0.2 MPa·m$^{1/2}$) (Fig. 3(g)). The work of fracture (WOF) was 510 ± 89 J·m^{-2} for C_3/CS-PVA, 1245 ± 136 J·m^{-2} for C_{30}/CS-PVA, 175 ± 48 J·m^{-2} for C_{120}/CS-PVA, and 2875 ± 285 J·m^{-2} for $C_{120\text{-}30\text{-}3}$/CS-PVA (Fig. 3(g)). The flexure strength of $C_{120\text{-}30\text{-}3}$/CS-PVA is comparable to nacre [39] and some PMMA/glass nanocomposites [35, 49, 51], but its K_{IC} is notably higher (Fig. 3(h)) [35, 39, 49, 51]. Although both flexural strength and K_{IC} are slightly lower than those of recently prepared PMMA/glass nanocomposites by mechanical vibration [52], the WOF is more than 5 times higher (Fig. 3(i)). It is likely the gradient architecture can enable more effective pathways for extrinsic toughening mechanisms [78] as mediated by the appropriate interface. With a comparable strength level [39, 51, 79], the WOF of $C_{120\text{-}30\text{-}3}$/CS-PVA is 7 times higher than PMMA/glass nanocomposites made by centrifugation [51], 11 times higher than silver-coated glass powder/PVA fabricated by pressing and sintering [79], and more than twice as high as nacre [39] (Fig. 3(i)). This exceptional WOF is even comparable to that of a conch shell (Fig. 3(i)) [80].

To investigate the impact of repeating patterns in gradient structures, laminates with varying aspect ratios of glass flakes every 10 and 70 layers were prepared, denoted as $C_{120(10)\text{-}30(10)\text{-}3(10)}$/CS-PVA and $C_{120(70)\text{-}30(70)\text{-}3(70)}$/CS-PVA, respectively (Figs. S13(a) and S13(b) in the ESM). It is important to note that these heterogeneous nanocomposites can be obtained by stacking different homogeneous films, which, however, is not feasible for the synthesis of $C_{120\text{-}30\text{-}3}$/CS-PVA. The flexural stress-strain curves revealed that $C_{120(70)\text{-}30(70)\text{-}3(70)}$/CS-PVA exhibited a flexural strength of 92.3 ± 4.9 MPa, a modulus of 2.2 ± 0.5 GPa, and a bending energy of 3.7 ± 0.9 MJ·m^{-3} (Fig. S14 in the ESM). In contrast, $C_{(120)10\text{-}(30)10\text{-}(3)10}$/CS-PVA showed a higher flexural strength of 118.9 ± 21.1 MPa, a modulus of 3.0 ± 0.4 GPa, and a bending energy of 5.8 ± 1.1 MJ·m^{-3} (Fig. S14 in the ESM). Notably, in these heterogeneous laminates, stress did not show the characteristic upturn after linear deformation, and there was no significant plastic deformation. Notched sample testing (Fig. S15 in the ESM) showed that the K_{IC} of $C_{120(10)\text{-}30(10)\text{-}3(10)}$/CS-PVA was 1.7 ± 0.5 MPa·m$^{1/2}$, which is higher than that of $C_{120(70)\text{-}30(70)\text{-}3(70)}$/CS-PVA (0.9 ± 0.3 MPa·m$^{1/2}$), but both are lower than the K_{IC} of $C_{120\text{-}30\text{-}3}$/CS-PVA (2.0 ± 0.6 MPa·m$^{1/2}$) (Fig. 3(g)). The WOF for $C_{120(10)\text{-}30(10)\text{-}3(10)}$/CS-PVA and $C_{120(70)\text{-}30(70)\text{-}3(70)}$/CS-PVA was measured at 1540 ± 195 and 515 ± 95 J·m^{-2}, respectively (Fig. 3(g)), both significantly lower than that of $C_{120\text{-}30\text{-}3}$/CS-PVA (2875 ± 285 J·m^{-2}) (Fig. 3(g)). These results underscore the crucial role of interfacial assembly in constructing gradient structures with significantly higher energy dissipation capabilities.

Finally, FEA simulations were conducted to model the three-point bending tests, both for notched and unnotched specimens. For homogeneous nanocomposites without a notch, the crack initially formed in C_{120}/CS-PVA (Fig. S16(a) in the ESM), consistent with its more localized stress distribution compared to C_{30}/CS-PVA and C_3/CS-PVA (Figs. S16(b) and S16(c) in the ESM). When a preexisting notch was introduced, the crack began to propagate first in C_{120}/CS-PVA as the loading increased (Fig. 4(a)). In contrast, the stress distribution in C_{30}/CS-PVA remained the farthest from the crack tip (Fig. 4(b)). As the load continued to increase, stress concentration at the crack area in C_3/CS-PVA led to crack propagation (Fig. 4(c)), whereas no crack growth was observed in C_{30}/CS-PVA (Fig. 4(b)).

For gradient structures, the stacking of C_{120}, C_{30}, and C_3 in a repeated sequence of 1 layer of glass flakes was used to mimic $C_{120\text{-}30\text{-}3}$/CS-PVA. In the unnotched case, during the loading process, stress initially concentrated in the region with glass flakes of high aspect ratio but gradually distributed across the glass flakes with lower aspect ratios (Fig. S17 in the ESM). This load transfer among glass flakes with different aspect ratios likely contributes to the increased stress observed after linear deformation (Fig. 3(d)). Further studies on repeated sequences of 2 and 3 were conducted. Without a notch, cracks appeared first in $C_{120\text{-}30\text{-}3}$/CS-PVA (repeated sequence of 3), likely due to a large stress concentration at the C_{120} (Fig. S18(a) in the ESM). In $C_{120\text{-}30\text{-}3}$/CS-PVA (repeated sequence of 2), cracks formed next (Fig. S18(b) in the ESM), whereas no cracks were observed in $C_{120\text{-}30\text{-}3}$/CS-PVA (repeated sequence of 1) (Fig. S18(c) in the ESM). The neighboring glass flakes with varying aspect ratios are expected to facilitate the delocalization of stress.

With a notch present, when the crack occurred in $C_{120\text{-}30\text{-}3}$/CS-PVA (repeated sequence of 3), the stress distribution was more uniform in $C_{120\text{-}30\text{-}3}$/CS-PVA (repeated sequence of 2) than in $C_{120\text{-}30\text{-}3}$/CS-PVA (repeated sequence of 1) (Figs. 4(d)–4(f)). Such difference led to slightly earlier crack expansion in $C_{120\text{-}30\text{-}3}$/CS-PVA (repeated sequence of 1) compared to $C_{120\text{-}30\text{-}3}$/CS-PVA (repeated sequence of 2) (Figs. 4(e) and 4(f)). However, because $C_{120\text{-}30\text{-}3}$/CS-PVA (repeated sequence of 1) could sustain a larger stress level (Fig. 4(g)), the energy consumed before force decline was highest for this configuration (Fig. 4(g)). A comparison with the homogeneous

structures (Fig. 4(h)) revealed that the gradient structures' effect was most pronounced in $C_{120\text{-}30\text{-}3}$/CS-PVA (repeated sequence of 1), which aligns with the experimental results (Fig. 3(g)). In contrast, when glass flakes of different aspect ratios were not in direct contact (such as in the repeated sequence of 3) (Fig. 4(g)), the energy consumed before the decline of force was smaller than that in the homogeneous counterparts (Fig. 4(h)).

4 Conclusions

In conclusion, surface silanization facilitates the interfacial assembly of glass flakes at the air-water interface, enabling precise structural control of nacre-like glass nanocomposites with high transparency and ultralow haze. The enhanced mechanical performance of the heterogeneous structures, which combine high strength and significant energy dissipation ability, is attributed to the effective stress delocalization mechanism enabled by the gradient architecture. The critical role of repeated sequences in achieving a synergetic effect is underscored by FEA simulations, which further emphasize the importance of interfacial assembly in precise structural control. Future work may focus on increasing the mass fraction of glass flakes and exploring other polymer systems, such as PMMA, to synthesize bioinspired gradient glass composites with improved properties.

Electronic Supplementary Material: Supplementary material (SEM images and TGA results of glass flakes/CS-PVA, elemental mappings, summaries of mechanical properties, the model and

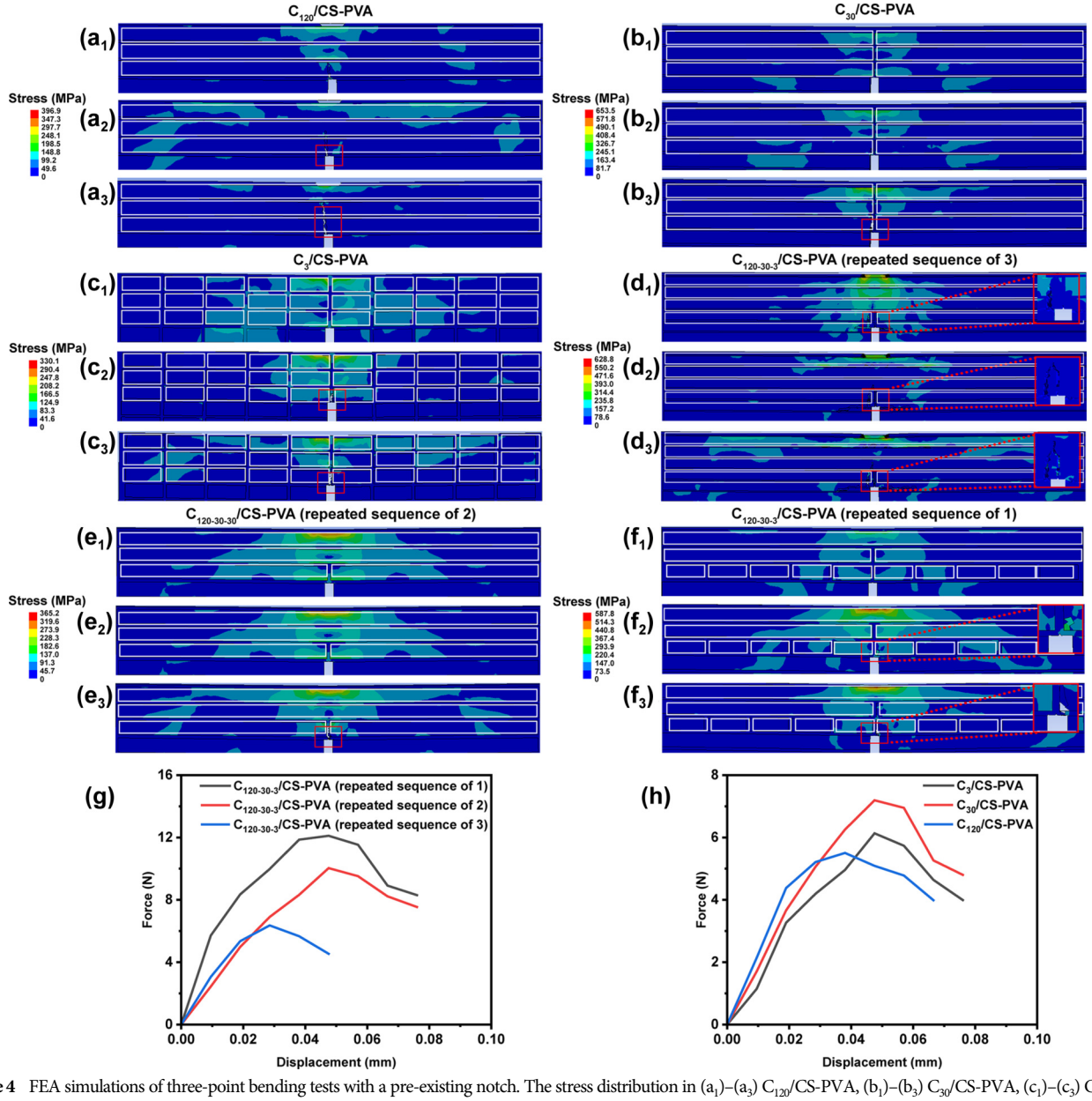

Figure 4 FEA simulations of three-point bending tests with a pre-existing notch. The stress distribution in (a_1)–(a_3) C_{120}/CS-PVA, (b_1)–(b_3) C_{30}/CS-PVA, (c_1)–(c_3) C_3/CS-PVA, (d_1)–(d_3) $C_{120\text{-}30\text{-}3}$/CS-PVA (repeated sequence of 3), (e_1)–(e_3) $C_{120\text{-}30\text{-}3}$/CS-PVA (repeated sequence of 2), and (f_1)–(f_3) $C_{120\text{-}30\text{-}3}$/CS-PVA (repeated sequence of 1) during simulated SENB tests. The simulated load–displacement curves of (g) $C_{120\text{-}30\text{-}3}$/CS-PVA (repeated sequence of 3), $C_{120\text{-}30\text{-}3}$/CS-PVA (repeated sequence of 2), and $C_{120\text{-}30\text{-}3}$/CS-PVA (repeated sequence of 1), and (h) C_{120}/CS-PVA, C_{30}/CS-PVA, and C_3/CS-PVA. For (a)–(f), from top to bottom, the load increases; in the same row, the load is the same.

results of FEA simulations, tensile and flexural stress–strain curves, load–displacement curves from SENB tests, and comparison of optical properties) is available in the online version of this article at https://doi.org/10.26599/NR.2025.94907173.

Data availability

All data needed to support the conclusions in the paper are presented in the manuscript and the Electronic Supplementary Material. Additional data related to this paper may be requested from the corresponding author upon request.

Acknowledgements

M. Y. thanks the National Natural Science Foundation of China (Nos. 22071075 and 22090044), and Research Foundation of Education Bureau of Jilin Province (No. JJKH20231134CY) for financial support.

Declaration of competing interest

All the contributing authors report no conflict of interests in this work.

Author contributions

C. Y. C.: Data curation, formal analysis, writing – original draft, writing – review & editing. J. Z.: Data curation. S. H. F.: Supervision. M. Y.: Conceptualization, methodology, writing – review & editing, supervision, project administration, funding acquisition. All the authors have approved the final manuscript.

Use of AI statement

During the preparation of this work, the authors used ChatGPT in order to improve the English writing.

References

[1] Liu, Z. Q.; Meyers, M. A.; Zhang, Z. F.; Ritchie, R. O. Functional gradients and heterogeneities in biological materials: Design principles, functions, and bioinspired applications. *Prog. Mater. Sci.* **2017**, *88*, 467–498.

[2] Quan, H. C.; Yang, W.; Lapeyriere, M.; Schaible, E.; Ritchie, R. O.; Meyers, M. A. Structure and mechanical adaptability of a modern elasmoid fish scale from the common carp. *Matter* **2020**, *3*, 842–863.

[3] Naleway, S. E.; Porter, M. M.; McKittrick, J.; Meyers, M. A. Structural design elements in biological materials: Application to bioinspiration. *Adv. Mater.* **2015**, *27*, 5455–5476.

[4] Barthelat, F.; Yin, Z.; Buehler, M. J. Structure and mechanics of interfaces in biological materials. *Nat. Rev. Mater.* **2016**, *1*, 16007.

[5] Nepal, D.; Kang, S.; Adstedt, K. M.; Kanhaiya, K.; Bockstaller, M. R.; Brinson, L. C.; Buehler, M. J.; Coveney, P. V.; Dayal, K.; El-Awady, J. A. et al. Hierarchically structured bioinspired nanocomposites. *Nat. Mater.* **2023**, *22*, 18–35.

[6] Zhang, Z. B.; Gao, H. L.; Wen, S. M.; Pang, J.; Zhang, S. C.; Cui, C.; Wang, Z. Y.; Yu, S. H. Scalable manufacturing of mechanical robust bioinspired ceramic-resin composites with locally tunable heterogeneous structures. *Adv. Mater.* **2023**, *35*, 2209510.

[7] Cao, R. Q.; Yu, Q.; Pan, J.; Lin, Y.; Sweet, A.; Li, Y.; Ritchie, R. O. On the exceptional damage-tolerance of gradient metallic materials. *Mater. Today* **2020**, *32*, 94–107.

[8] Shang, Z. X.; Sun, T. Y.; Ding, J.; Richter, N. A.; Heckman, N. M.; White, B. C.; Boyce, B. L.; Hattar, K.; Wang, H. Y.; Zhang, X. H. Gradient nanostructured steel with superior tensile plasticity. *Sci. Adv.* **2023**, *9*, eadd9780.

[9] Cao, J.; Zhou, Z. H.; Song, Q. C.; Chen, K. Y.; Su, G. H.; Zhou, T.; Zheng, Z.; Lu, C. H.; Zhang, X. X. Ultrarobust $Ti_3C_2T_x$ MXene-based soft actuators via bamboo-inspired mesoscale assembly of hybrid nanostructures. *ACS Nano* **2020**, *14*, 7055–7065.

[10] Libanori, R.; Erb, R. M.; Reiser, A.; Le Ferrand, H.; Süess, M. J.; Spolenak, R.; Studart, A. R. Stretchable heterogeneous composites with extreme mechanical gradients. *Nat. Commun.* **2012**, *3*, 1265.

[11] Liu, Z. Y.; Qi, D. P.; Guo, P. Z.; Liu, Y.; Zhu, B. W.; Yang, H.; Liu, Y. Q.; Li, B.; Zhang, C. G.; Yu, J. C. et al. Thickness-gradient films for high gauge factor stretchable strain sensors. *Adv. Mater.* **2015**, *27*, 6230–6237.

[12] Pragya, A.; Ghosh, T. K. Soft functionally gradient materials and structures-natural and manmade: A review. *Adv. Mater.* **2023**, *35*, 2300912.

[13] Giachini, P. A. G. S.; Gupta, S. S.; Wang, W.; Wood, D.; Yunusa, M.; Baharlou, E.; Sitti, M.; Menges, A. Additive manufacturing of cellulose-based materials with continuous, multidirectional stiffness gradients. *Sci. Adv.* **2020**, *6*, eaay0929.

[14] Wegst, U. G. K.; Bai, H.; Saiz, E.; Tomsia, A. P.; Ritchie, R. O. Bioinspired structural materials. *Nat. Mater.* **2015**, *14*, 23–36.

[15] Finnemore, A.; Cunha, P.; Shean, T.; Vignolini, S.; Guldin, S.; Oyen, M.; Steiner, U. Biomimetic layer-by-layer assembly of artificial nacre. *Nat. Commun.* **2012**, *3*, 996.

[16] Mao, L. B.; Gao, H. L.; Yao, H. B.; Liu, L.; Cölfen, H.; Liu, G.; Chen, S. M.; Li, S. K.; Yan, Y. X.; Liu, Y. Y. et al. Synthetic nacre by predesigned matrix-directed mineralization. *Science* **2016**, *354*, 107–110.

[17] Cheng, Q. F.; Jiang, L.; Tang, Z. Y. Bioinspired layered materials with superior mechanical performance. *Acc. Chem. Res.* **2014**, *47*, 1256–1266.

[18] Tang, Z. Y.; Kotov, N. A.; Magonov, S.; Ozturk, B. Nanostructured artificial nacre. *Nat. Mater.* **2003**, *2*, 413–418.

[19] Zhao, H. W.; Yang, Z.; Guo, L. Nacre-inspired composites with different macroscopic dimensions: Strategies for improved mechanical performance and applications. *NPG Asia Mater.* **2018**, *10*, 1–22.

[20] Espinosa, H. D.; Juster, A. L.; Latourte, F. J.; Loh, O. Y.; Gregoire, D.; Zavattieri, P. D. Tablet-level origin of toughening in abalone shells and translation to synthetic composite materials. *Nat. Commun.* **2011**, *2*, 173.

[21] Xu, Z. H.; Li, X. D. Deformation strengthening of biopolymer in nacre. *Adv. Funct. Mater.* **2011**, *21*, 3883–3888.

[22] Song, F.; Soh, A. K.; Bai, Y. L. Structural and mechanical properties of the organic matrix layers of nacre. *Biomaterials* **2003**, *24*, 3623–3631.

[23] Gim, J.; Schnitzer, N.; Otter, L. M.; Cui, Y. C.; Motreuil, S.; Marin, F.; Wolf, S. E.; Jacob, D. E.; Misra, A.; Hovden, R. Nanoscale deformation mechanics reveal resilience in nacre of *Pinna nobilis* shell. *Nat. Commun.* **2019**, *10*, 4822.

[24] Zhao, C. Q.; Zhang, P. C.; Zhou, J. J.; Qi, S. H.; Yamauchi, Y.; Shi, R. R.; Fang, R. C.; Ishida, Y.; Wang, S. T.; Tomsia, A. P. et al. Layered nanocomposites by shear-flow-induced alignment of nanosheets. *Nature* **2020**, *580*, 210–215.

[25] Podsiadlo, P.; Kaushik, A. K.; Arruda, E. M.; Waas, A. M.; Shim, B. S.; Xu, J. D.; Nandivada, H.; Pumplin, B. G.; Lahann, J.; Ramamoorthy, A. et al. Ultrastrong and stiff layered polymer nanocomposites. *Science* **2007**, *318*, 80–83.

[26] Chen, K.; Tang, X. K.; Jia, B. B.; Chao, C. Z.; Wei, Y.; Hou, J. Y.; Dong, L. T.; Deng, X. L.; Xiao, T. H.; Goda, K. et al. Graphene oxide bulk material reinforced by heterophase platelets with multiscale interface crosslinking. *Nat. Mater.* **2022**, *21*, 1121–1129.

[27] Cui, W.; Li, M. Z.; Liu, J. Y.; Wang, B.; Zhang, C.; Jiang, L.; Cheng, Q. F. A strong integrated strength and toughness artificial nacre based on dopamine cross-linked graphene oxide. *ACS Nano* **2014**, *8*, 9511–9517.

[28] Li, Y. Q.; Yu, T.; Yang, T. Y.; Zheng, L. X.; Liao, K. Bio-inspired nacre-like composite films based on graphene with superior mechanical, electrical, and biocompatible properties. *Adv. Mater.* **2012**, *24*, 3426–3431.
[29] Wang, H. G.; Lu, R. J.; Li, L.; Liang, C.; Yan, J.; Liang, R.; Sun, G. X.; Jiang, L.; Cheng, Q. F. Strong, tough, and thermally conductive nacre-inspired boron nitride nanosheet/epoxy layered nanocomposites. *Nano Res.* **2024**, *17*, 820–828.
[30] Yoo, S. C.; Park, Y. K.; Park, C.; Ryu, H.; Hong, S. H. Biomimetic artificial nacre: Boron nitride nanosheets/gelatin nanocomposites for biomedical applications. *Adv. Funct. Mater.* **2018**, *28*, 1805948.
[31] Cao, W. T.; Chen, F. F.; Zhu, Y. J.; Zhang, Y. G.; Jiang, Y. Y.; Ma, M. G.; Chen, F. Binary strengthening and toughening of MXene/cellulose nanofiber composite paper with nacre-inspired structure and superior electromagnetic interference shielding properties. *ACS Nano* **2018**, *12*, 4583–4593.
[32] Yan, J.; Zhou, T. Z.; Yang, X. Y.; Zhang, Z. J.; Li, L.; Zou, Z. Y.; Fu, Z. Y.; Cheng, Q. F. Strong and tough MXene bridging-induced conductive nacre. *Angew. Chem., Int. Ed.* **2024**, *63*, e202405228.
[33] Wang, J. E.; Song, T. L.; Ming, W.; Yele, M.; Chen, L. F.; Zhang, H.; Zhang, X. J.; Liang, B. L.; Wang, G. S. High MXene loading, nacre-inspired MXene/ANF electromagnetic interference shielding composite films with ultralong strain-to-failure and excellent joule heating performance. *Nano Res.* **2024**, *17*, 2061–2069.
[34] Munch, E.; Launey, M. E.; Alsem, D. H.; Saiz, E.; Tomsia, A. P.; Ritchie, R. O. Tough, bio-inspired hybrid materials. *Science* **2008**, *322*, 1516–1520.
[35] Magrini, T.; Bouville, F.; Lauria, A.; Le Ferrand, H.; Niebel, T. P.; Studart, A. R. Transparent and tough bulk composites inspired by nacre. *Nat. Commun.* **2019**, *10*, 2794.
[36] Eckert, A.; Rudolph, T.; Guo, J. Q.; Mang, T.; Walther, A. Exceptionally ductile and tough biomimetic artificial nacre with gas barrier function. *Adv. Mater.* **2018**, *30*, 1802477.
[37] Liu, Z. Q.; Zhu, Y. K.; Jiao, D.; Weng, Z. Y.; Zhang, Z. F.; Ritchie, R. O. Enhanced protective role in materials with gradient structural orientations: Lessons from nature. *Acta Biomater.* **2016**, *44*, 31–40.
[38] Huang, W.; Restrepo, D.; Jung, J. Y.; Su, F. Y.; Liu, Z. Q.; Ritchie, R. O.; McKittrick, J.; Zavattieri, P.; Kisailus, D. Multiscale toughening mechanisms in biological materials and bioinspired designs. *Adv. Mater.* **2019**, *31*, 1901561.
[39] Madhav, D.; Buffel, B.; Moldenaers, P.; Desplentere, F.; Vandeginste, V. A review of nacre-inspired materials: Chemistry, strengthening-deformation mechanism, synthesis, and applications. *Prog. Mater. Sci.* **2023**, *139*, 101168.
[40] Li, X. D.; Chang, W. C.; Chao, Y. J.; Wang, R. Z.; Chang, M. Nanoscale structural and mechanical characterization of a natural nanocomposite material: The shell of red abalone. *Nano Lett.* **2004**, *4*, 613–617.
[41] Yang, H. M.; Jo, S.; Oh, J. H.; Choi, B. H.; Woo, J. Y.; Han, C. S. Strong and tough nacre-inspired graphene oxide composite with hierarchically similar structure. *ACS Nano* **2022**, *16*, 10509–10516.
[42] Woigk, W.; Poloni, E.; Grossman, M.; Bouville, F.; Masania, K.; Studart, A. R. Nacre-like composites with superior specific damping performance. *Proc. Natl. Acad. Sci. USA* **2022**, *119*, e2118868119.
[43] Wu, Z. Y.; Pan, H.; Huang, P.; Tang, J. H.; She, W. Biomimetic mechanical robust cement-resin composites with machine learning-assisted gradient hierarchical structures. *Adv. Mater.* **2024**, *36*, 2405183.
[44] Meng, Y. F.; Yu, C. X.; Zhou, L. C.; Shang, L. M.; Yang, B.; Wang, Q. Y.; Meng, X. S.; Mao, L. B.; Yu, S. H. Nanograded artificial nacre with efficient energy dissipation. *Innovation* **2023**, *4*, 100505.
[45] Abid, N.; Mirkhalaf, M.; Barthelat, F. Discrete-element modeling of nacre-like materials: Effects of random microstructures on strain localization and mechanical performance. *J. Mech. Phys. Solids* **2018**, *112*, 385–402.
[46] Jiang, M. Y.; Meng, X. Y.; Zhou, J.; Wei, Z. Y.; Zhang, H. F.; Shen, P. Design and manufacture of near-net-shape metal-ceramic composites with gradient-layered structure and optimized damage tolerance. *Addit. Manuf.* **2024**, *84*, 104112.
[47] Wei, Z. Q.; Xu, X. H. Gradient design of bio-inspired nacre-like composites for improved impact resistance. *Compos. B Eng.* **2021**, *215*, 108830.
[48] Bouville, F.; Maire, E.; Meille, S.; Van de Moortèle, B.; Stevenson, A. J.; Deville, S. Strong, tough and stiff bioinspired ceramics from brittle constituents. *Nat. Mater.* **2014**, *13*, 508–514.
[49] Magrini, T.; Moser, S.; Fellner, M.; Lauria, A.; Bouville, F.; Studart, A. R. Transparent nacre-like composites toughened through mineral bridges. *Adv. Funct. Mater.* **2020**, *30*, 2002149.
[50] Yin, Z.; Hannard, F.; Barthelat, F. Impact-resistant nacre-like transparent materials. *Science* **2019**, *364*, 1260–1263.
[51] Amini, A.; Khavari, A.; Barthelat, F.; Ehrlicher, A. J. Centrifugation and index matching yield a strong and transparent bioinspired nacreous composite. *Science* **2021**, *373*, 1229–1234.
[52] Amini, A.; Tirgar, P.; Bahmani, A.; Jafari, M.; Siaj, M.; Barthelat, F.; Ehrlicher, A. Nacreous glass composites with superior performance engineered through mechanical vibration and silanization. *Adv. Funct. Mater.* **2024**, *34*, 2405008.
[53] Shim, J.; Yun, J. M.; Yun, T.; Kim, P.; Lee, K. E.; Lee, W. J.; Ryoo, R.; Pine, D. J.; Yi, G. R.; Kim, S. O. Two-minute assembly of pristine large-area graphene based films. *Nano Lett.* **2014**, *14*, 1388–1393.
[54] Ariga, K.; Yamauchi, Y.; Mori, T.; Hill, J. P. 25th Anniversary article: What can be done with the Langmuir-Blodgett method. Recent developments and its critical role in materials science. *Adv. Mater.* **2013**, *25*, 6477–6512.
[55] Bonderer, L. J.; Studart, A. R.; Gauckler, L. J. Bioinspired design and assembly of platelet reinforced polymer films. *Science* **2008**, *319*, 1069–1073.
[56] He, Z.; Wang, J. L.; Chen, S. M.; Liu, J. W.; Yu, S. H. Self-assembly of nanowires: From dynamic monitoring to precision control. *Acc. Chem. Res.* **2022**, *55*, 1480–1491.
[57] Wan, S. J.; Jiang, L.; Cheng, Q. F. Design principles of high-performance graphene films: Interfaces and alignment. *Matter* **2020**, *3*, 696–707.
[58] Zhang, C. Interfacial assembly of two-dimensional MXenes. *J. Energy Chem.* **2021**, *60*, 417–434.
[59] Yu, Z. B.; Du, X. M.; Zhu, P. L.; Zhao, T.; Sun, R.; Chen, J. Z.; Wang, N.; Li, W. H. Surface modified hollow glass microspheres-epoxy composites with enhanced thermal insulation and reduced dielectric constant. *Mater. Today Commun.* **2022**, *32*, 104046.
[60] Zhang, W. Q.; Wang, B. B.; Xu, X. W.; Feng, H. Z.; Hu, K. Z.; Su, Y.; Zhou, S. C.; Zhu, J.; Weng, G. S.; Ma, S. Q. Green and facile method for valorization of lignin to high-performance degradable thermosets. *Green Chem.* **2022**, *24*, 9659–9667.
[61] Xu, M. H.; Pan, G. X.; Guo, Y. H.; Yang, S. C.; Fang, Z. Surface modification and structure analysis of coated iron oxide yellow pigments to improve dispersion in organic solvents. *Surf. Interface Anal.* **2021**, *53*, 933–945.
[62] Chen, X.; Li, G. Q.; Głodek, M.; Knozowska, K.; Kujawa, J.; Zhang, P. C.; Kujawski, W. Efficient surface engineering of aluminum foil by using piranha solution strategy. *Surf. Interfaces* **2023**, *43*, 103566.
[63] Baidya, A.; Ganayee, M. A.; Ravindran, S. J.; Tam, K. C.; Das, S. K.; Ras, R. H. A.; Pradeep, T. Organic solvent-free fabrication of durable and multifunctional superhydrophobic paper from waterborne fluorinated cellulose nanofiber building blocks. *ACS Nano* **2017**, *11*, 11091–11099.
[64] Yu, Z.; Li, B. D.; Chu, J. Y.; Zhang, P. F. Silica *in situ* enhanced PVA/chitosan biodegradable films for food packages. *Carbohydr. Polym.* **2018**, *184*, 214–220.
[65] Guner, S. N. G.; Dericioglu, A. F. Nacre-mimetic bulk lamellar composites reinforced with high aspect ratio glass flakes. *Bioinspir. Biomim.* **2017**, *12*, 016002.

[66] Cano, M.; Khan, U.; Sainsbury, T.; O'Neill, A.; Wang, Z. M.; McGovern, I. T.; Maser, W. K.; Benito, A. M.; Coleman, J. N. Improving the mechanical properties of graphene oxide based materials by covalent attachment of polymer chains. *Carbon* **2013**, *52*, 363–371.

[67] Zeng, X. L.; Ye, L.; Yu, S. H.; Li, H.; Sun, R.; Xu, J. B.; Wong, C. P. Artificial nacre-like papers based on noncovalent functionalized boron nitride nanosheets with excellent mechanical and thermally conductive properties. *Nanoscale* **2015**, *7*, 6774–6781.

[68] Liang, B. L.; Shu, Y. Q.; Wan, P.; Zhao, H. W.; Dong, S. H.; Hao, W. C.; Yin, P. G. Genipin-enhanced nacre-inspired montmorillonite-chitosan film with superior mechanical and UV-blocking properties. *Compos. Sci. Technol.* **2019**, *182*, 107747.

[69] Yao, H. B.; Fang, H. Y.; Tan, Z. H.; Wu, L. H.; Yu, S. H. Biologically inspired, strong, transparent, and functional layered organic–inorganic hybrid films. *Angew. Chem., Int. Ed.* **2010**, *49*, 2140–2145.

[70] Shu, Y. Q.; Yin, P. G.; Liang, B. L.; Wang, H.; Guo, L. Bioinspired design and assembly of layered double hydroxide/poly(vinyl alcohol) film with high mechanical performance. *ACS Appl. Mater. Interfaces* **2014**, *6*, 15154–15161.

[71] Channa, I. A.; Ashfaq, J.; Gilani, S. J.; Chandio, A. D.; Yousuf, S.; Makhdoom, M. A.; bin Jumah, M. N. Sustainable and eco-friendly packaging films based on poly (vinyl alcohol) and glass flakes. *Membranes* **2022**, *12*, 701.

[72] Yu, Y. D.; Kong, K. R.; Tang, R. K.; Liu, Z. M. A bioinspired ultratough composite produced by integration of inorganic ionic oligomers within polymer networks. *ACS Nano* **2022**, *16*, 7926–7936.

[73] Gao, H. L.; Chen, S. M.; Mao, L. B.; Song, Z. Q.; Yao, H. B.; Cölfen, H.; Luo, X. S.; Zhang, F.; Pan, Z.; Meng, Y. F. et al. Mass production of bulk artificial nacre with excellent mechanical properties. *Nat. Commun.* **2017**, *8*, 287.

[74] Lossada, F.; Zhu, B. L.; Walther, A. Dry processing and recycling of thick nacre-mimetic nanocomposites. *Adv. Funct. Mater.* **2021**, *31*, 2102677.

[75] Lossada, F.; Jiao, D. J.; Hoenders, D.; Walther, A. Recyclable and light-adaptive vitrimer-based nacre-mimetic nanocomposites. *ACS Nano* **2021**, *15*, 5043–5055.

[76] Verho, T.; Karppinen, P.; Gröschel, A. H.; Ikkala, O. Imaging inelastic fracture processes in biomimetic nanocomposites and nacre by laser speckle for better toughness. *Adv. Sci.* **2018**, *5*, 1700635.

[77] Pan, H.; She, W.; Zuo, W. Q.; Zhou, Y.; Huang, J. L.; Zhang, Z. W.; Geng, Z. F.; Yao, Y. M.; Zhang, W. H.; Zheng, L. et al. Hierarchical toughening of a biomimetic bulk cement composite. *ACS Appl. Mater. Interfaces* **2020**, *12*, 53297–53309.

[78] Ritchie, R. O. Toughening materials: Enhancing resistance to fracture. *Philos. Trans. A Math Phys. Eng. Sci.* **2021**, *379*, 20200437.

[79] Kakisawa, H.; Sumitomo, T.; Inoue, R.; Kagawa, Y. Fabrication of nature-inspired bulk laminar composites by a powder processing. *Compos. Sci. Technol.* **2010**, *70*, 161–166.

[80] Li, M.; Zhao, N. F.; Wang, M. N.; Dai, X. G.; Bai, H. Conch-shell-inspired tough ceramic. *Adv. Funct. Mater.* **2022**, *32*, 2205309.